Cav03-GS-12-003

Fifth International Symposium on Cavitation (CAV2003)
Osaka, Japan, November 1-4, 2003

TIP LEAKAGE VORTEX (TLV) VARIABILITY FROM A DUCTED PROPELLER UNDER STEADY OPERATION AND ITS IMPLICATIONS ON CAVITATION INCEPTION

Ghanem Oweis
University of Michigan
goweis@umich.edu

Steven Ceccio
University of Michigan
ceccio@umich.edu

Christopher Chesnakas
Naval Surface Warfare Center
ChesnakasCJ@nswccd.navy.mil

David Fry
Naval Surface Warfare Center
FryDJ@nswccd.navy.mil

Stuart Jessup
Naval Surface Warfare Center
JessupSD@nswccd.navy.mil

ABSTRACT

The flow in the close vicinity of the blade-tip region of ducted propellers and similar hydro-machines can be quite complex due to the presence and dynamic interactions of the tip-leakage vortex (TLV), the blade trailing edge vortex, (TEV) the gap shear flow, the wall (casing) boundary layer, and the wake from the blade boundary layer. This tip region flow is important as it has the potential to contribute to a substantial loss in total efficiency and pumping head. In hydro-machinery, there is the additional issue of cavitation. In the present study, Laser Doppler Velocimetry (LDV) and Particle Imaging Velocimetry (PIV) measurements were performed on the TLV from a ducted marine propulsor 33.4" in diameter at the blade TEV under steady operating conditions. The measurements were synchronized with the propeller angular position. Analysis of the velocity fields revealed considerable variations among the instantaneous realizations at a given spatial position in the tip vortex strength, its core size, and its overall structure. The implications of vortex variability on cavitation inception are discussed. In addition, significant differences exist between the averaged vortex properties from the instantaneous flow fields and the averaged vortex properties from the mean flow field. We will discuss these differences and their influence on cavitation performance and scaling.

INTRODUCTION

A series of experiments have been conducted to understand the inception and scaling of discrete cavitation in the tip region of two geometrically similar ducted propulsor. Chesnakas and Jessup (2003) [1] reported some results from three-component Laser Doppler Velocimetry (LDV) measurements. The inception of limited event rate cavitation was also examined and reported.

Presented here are some results from planar Particle Imaging Velocimetry (PIV) measurements performed downstream of the rotor in the tip region. These measurements were used to evaluate the instantaneous flow fields and their variability. The process of vortex roll-up is examined as the primary tip leakage vortex merges with a trailing edge vortex and other, weaker vortices in the blade wake spiral (mean flow field measurements). This flow has significant variability, and we will examine how the average and statistical characteristics of the tip-leakage flow vary with Reynolds number.

NOMENCLATURE

ΔP: difference between the vortex centerline pressure and the free stream pressure.
R_V^2 : regression value measuring the goodness of fit for the velocity field.
R_ω^2: regression value measuring the goodness of fit for the vorticity field.
$\overline{u'}^2$:vortex field velocity fluctuations in the axial direction.
$\overline{v'}^2$:vortex field velocity fluctuations in the radial direction.
a: vortex core size.
c: chord length
C_L: lift coefficient.
C_P: pressure coefficient.
D: propeller tip diameter ($2\times R_P$)
f: blade camber.
fps: foot per second.
G: average circulation in the rotor wake.
g: tip clearance.
i_T: blade total rake.
J: advance ratio.
K_Q: thrust coefficient.
K_T: torque coefficient.
n: propeller RPM.
P_∞: static pressure in the test section.
p: blade pitch.
Q: thrust.

R: propeller radius (to the blade tip).
r: radial distance measured from the propeller axis of rotation. Also radial distance from the vortex center.
s: pitch line (propeller angular speed × R_P × time separation)
t: blade maximum thickness at the tip.
T: torque.
U_∞: tunnel free stream velocity.
u_θ: vortex tangential velocity.
U_c: vortex core mean tangential velocity.
U_x: tunnel axial velocity (parallel to propeller axis of rotation.)
x: axial distance parallel to the propeller axis of rotation.
Z: number of blades (3).
ρ and ρ_f: water density.
κ: standard deviation of vortex position variation (wandering).
ω: vorticity.
η_1: constant (1.257).
δ_1: duct boundary layer thickness.
η_2: constant (0.715).
η_3: constant of integration (0.870).
ω_c: vortex core mean vorticity.
σ_i: cavitation inception number.
θ_s: skew angle.
$\Gamma(r)$: vortex circulation as a function of radius.
Γ_0: vortex total circulation (from r = 0 to r = ∞)

EXPERIMENTAL SETUP

The experiments were performed in the David Taylor 36-inch Variable Pressure Cavitation Tunnel. The 36-inch diameter, open jet test section was used for these tests. For these studies, the propeller was driven using the upstream dynamometer. Inflow to the propeller was uniform except for the wakes from three upstream shaft support struts. Two geometrically similar, ducted, 3-bladed rotors were tested in this investigation (Figure 1). The larger rotor, Propeller 5206, was sized to be the maximum possible size to fit into the 36-Inch water tunnel. The rotor had a hub diameter of 13.847 in. (0.3517 m), a tip diameter of 33.475 in. (0.8503m), and a constant chord of 15.008 in. (0.3812 m) from hub to tip. It operated in a duct of diameter 34.00 in. (0.8636m), placed in the open jet nozzle so that the entire tunnel flow went through the propulsor. The straight portion of the duct had a linear extent of 25.5 in (X m) and extended from –19 in to + 6.5 in, where *R* is the rotor radius.

The smaller rotor, Propeller 5407, had a hub diameter of 4.964 in. (0.1261m), a tip diameter of 12.000 in. (0.3048m), and operated in a duct of diameter 12.188 in. (0.3096m). The duct of the small rotor had an inside diameter of 12.188 in (0.3096 m), an outer diameter of 13.215 in (0.3352 m), and a linear extent of 27.5 in (0.6985 m). It was positioned from –4.36 *x/R* to 0.598 *x/R*. A bell-mouth was installed on the inlet of the duct with a 3.00 in (0.076 m) radius on the inner and outer walls. The length scale ratio of the two rotors was 2.790.

The rotor geometry is detailed in Table 1. To identify where boundary layer transition would affect the results, boundary layer trips were placed on some blades. For most measurements, no influence of the boundary layer trips was noted. The ratio of the tip clearance to the maximum thickness at the tip, *g/t*, was 0.17, which is near the optimum value of 0.2 reported by Farrell and Billet (1994) [2] to reduce the potential for tip-leakage cavitation. The propeller was made using a numerically controlled milling process and manufactured to tolerances of approximately 0.1 mm from a mono-bloc 6061T6 aluminum forging. The blade section was a NACA 66, DTMB (David Taylor Model Basin) modified thickness form, with a 0.8 mean-line camber, with trailing edges thickened to incorporate a typical anti-singing trailing edge bevel. The blade pitch was reduced at the hub and tip to minimize root and tip cavitation.

A window was inserted into the duct to allow for optical access to the rotor flow, as shown in Figure 1a and 1b. The installation of the widow produced a pocket in the duct. While no flow passed through the window, the presence of the pocket was not entirely passive. Laser Doppler Velocimetry (LDV) measurements performed by Chesnakas and Jessup (2003) [1] showed that the primary vortex moved in and out of the cavity as the rotor blade passed by. However, this effect was not so pronounced to significantly alter the character of the flow in the tip region. The LDV was also used to measure the inlet flow profile upstream of the rotors through a transparent window placed in the duct.

A planar Particle Imaging Velocimetry (PIV) system was implemented for use in the water tunnel. Figure 1a and 1b show a schematic drawing of the PIV setup. The light sheet was produced by two lasers operating outside the test-section, while the digital camera used to record the low images was mounted in a waterproof housing within the still-water region of the test section. Two Quanta-Ray PRO-250 Series Pulsed Nd:YAG lasers with pulse energy up to 800 mJ/pulse at 532 nm were used to created a double-pulsed light sheet. The two beams were combined and formed into a light sheet of 5 mm thickness and double pulsed with a time separation varying between 6 ms and 20 ms for differing propeller speeds and distances from the blade trailing edge. The light sheet passed through windows in the outer wall of the test section and through the transparent duct pocket to illuminate the flow. The sheet was oriented parallel to the propeller-shaft axis, as shown in Figure 1b. The radial and axial positions of the camera were moved to place the mean center of the vortex in the center of the image. The whole tunnel was seeded before the start of the experiments with Silicon Carbide particles of 1 micron mean diameter. A LaVision FlowMaster-3S PIV/PTV system was used to control the firing of the lasers and synchronize image capture with a CCD digital imager.

r/R_P	c/D	p/D	i_T/D	t/c	f/c	θ_s
0.416	0.446	0.92	-0.0063	0.172	-0.065	-0.4°
0.5	0.446	1.135	0.0063	0.148	0.000	4.2°
0.6	0.446	1.220	0.0145	0.119	0.037	10.0°
0.7	0.446	1.175	0.0227	0.102	0.047	15.9°
0.8	0.446	1.087	0.0309	0.100	0.047	21.5°
0.9	0.446	0.995	0.0391	0.100	0.038	26.3°
1.0	0.446	0.905	0.0473	0.100	0.020	30.0°

Table 1: Geometry of the rotors. The radial dimension is *r*, the rotor radius is R_P, and the diameter is *D*. The chord is *c*, the

pitch is p, the total rake is i_T, the maximum thickness is t, the camber is f, and the skew angle is θ_s.

The imager was a 1280 by 1024 pixel cross-correlation camera with 12-bit resolution and 4 Hz repetition rate in the cross correlation mode. The camera axis was perpendicular to the laser sheet and recorded the in-plane motion of the tracer particles. The light sheet was sufficiently thick to reduce the number of particles that entered or exited the light sheet due to possible strong cross-plane flow velocities. The image field-of-view was 37.7 by 29.6 mm, and the lenses on the camera were chosen to have a depth-of-field much larger than the thickness of the light sheet. The images were spatially calibrated by taking images of a registration target in the image plane. Images of the target were taken in the filled test section. A multi-pass algorithm was used to create in-plane velocity vectors using 32 pixel interrogation windows with 15% overlap applied in the final pass. This produced a velocity field with 46 by 37 vectors at 0.83 mm vector spacing. Timing of the PIV image capture was synchronized with the passage of the rotor blades, making it possible to capture multiple images at a given blade position. For the small rotor, the field of view was 11.76 by 9.35 mm and the vector spacing was 0.302 mm. The images were taken at various downstream distances along the pitch line, s, with $s = 0$ at the trailing edge and tip of the selected blade. The distance s was the product of the propeller tip tangential velocity and the time separation from the blade trailing edge to the PIV imaging plane. The velocity vectors were used to compute the vorticity field by making use of Stokes theorem. The vorticity at a point was calculated from the line integral of the velocity vector around a closed loop surrounding the point under consideration divided by the total area enclosed. On the experimental grid, the integration loop was composed of line segments chosen to pass through the centers of the 8 neighboring cells surrounding the cell of interest. On the rims of the PIV grid, vorticity was calculated using forward and backward differentiation schemes. After the vorticity field was calculated, a 3 by 3 mean filter was used to reduce noise.

The rotor was operated at a constant advance coefficient ($J = U_\infty / nD$) where U_∞ is the average flow speed into the duct, n is the rotational speed of the rotor, and D is the rotor diameter. The operating advance coefficient was selected to produce a typical leakage vortex, without unwanted flow conditions over the blade, with $J = 0.971$. This is higher than the design advanced coefficient in order to avoid the formation of the leakage vortex at the leading edge of the blade and the occurrence of pressure side leading edge cavitation near the blade tip. Several rotational speeds were examined for both rotors. The blade-tip Reynolds number is based on the chord, c, and the total tip speed, $(U_\infty + \pi Dn)$. The water kinematic viscosity was evaluated at the average flow temperature. The inlet absolute static pressure was maintained high enough (P_∞= 309 kPa at 500 RPM) during the PIV measurements to suppress cavitation. This advance coefficient resulted in a thrust coefficient $K_T = T / \rho n^2 D^4$ = 0.31 and a torque coefficient $K_Q = Q / \rho n^2 D^5$ = 0.54 that did not significantly vary over the range of Reynolds numbers studied. Application of roughness to the leading edge of the rotor blades did not significantly influence the measured results. Table 2 presents conditions reported here for both rotor configurations.

	U_∞ *(fps,[m/s])*	*n (RPM)*	*Reynolds#*
5407 Rotor "Small"	4.4 [1.34]	300	0.7 x 10^6
	8.8 [2.68]	600	1.4 x 10^6
	17.6 [5.36]	1200	2.8 x 10^6
	26.3 [8.02]	1800	4.3 x 10^6
5206 Rotor "Large"	10.2 [3.11]	250	4.6 x 10^6
	12.8 [3.90]	313	5.8 x 10^6
	15.3 [4.66]	375	6.9 x 10^6
	17.9 [5.46]	438	8.1 x 10^6
	20.4 [6.22]	500	9.2 x 10^6

Table 2: Test conditions for the 5407 and 5206 rotor configurations. The advance coefficient was constant at J = 0.971. The Reynolds number is based on the chord, c, and the total tip speed, $(U_\infty + \pi Dn)$.

The geometrical tolerance of the machined rotors is 0.1 mm. Variability of the rotor gap was +/- 0.030 in (0.76 mm) for the 5407 rotor and +/- 0.063 in (1.6 mm) for the 5206 rotor assemblies. The uncertainty associated with the measurements of test parameters (i.e. rotor speed, free-stream speed, free-stream pressure and temperature, rotor thrust, and rotor torque) are less than +/- 1%. Uncertainty of the presented LDV measurements is +/- 0.8%. The accumulated uncertainty of the PIV velocity measurements are less than +/- 5% with a spatial accuracy of +/- 0.03 mm for measurements of the large rotor and +/- 0.009 mm for measurements of the small rotor (pixel size).

INLET FLOW

The inlet axial velocity, U_x / U_∞, and tangential velocity, U_T, profiles were measured in the duct at x/R_P = -0.3615 and is plotted in Figure 3 for the case of 1200 rpm on the small rotor and 500 rpm on the large rotor. For both rotors the axial velocity is nearly constant from $0.5 \le r/R_P \le 0.9$. The wall boundary layer, however, is about 50% thicker for the small rotor (δ_1/R_P = 0.090) than for the large rotor (δ_1/R_P = 0.060). Note that for both rotors the duct boundary-layer thickness is much larger than the tip gap of g/R_P = 0.015. The small gap of the small rotor is nearly 1/6 times the inlet boundary layer, and the gap on the large rotor is 1/4 the boundary layer thickness.

Both rotors have a small amount of swirl in the inflow, with the large rotor having a small negative tangential velocity (opposite the direction of rotor rotation) and the small rotor having a small positive tangential velocity.

OVERALL DEVELOPMENT OF THE TIP-LEAKAGE FLOW

Both LDV measurements performed by Chesnakas and Jessup (2003) [1] and the PIV measurements discuss here reveal the general development of the flow in the tip region of the rotor operating at the given advanced coefficient. The pressure difference across the blade produces a flow through the tip region and the formation of a strong tip-leakage vortex, which we will refer to as the primary vortex. A second co-rotating concentrated vortex forms at the trailing edge, and we will refer to this as the secondary vortex. Additionally, there were multiple secondary co-rotating vortices of comparable or weaker strength. Counter-rotating secondary vortices were also present. Figure 4 shows the primary and secondary vortices visualized by cavitation in their respective cores. In addition, concentrated vorticity is also present in the blade wake. The mean axes of the primary and secondary vortices are not necessarily perpendicular to the plane made by the PIV light sheet, but the largest portion of the vorticity is in this plane, as discussed below. At increasing downstream distances from the blade trailing edge, these vortices begin to orbit and merge together.

Figure 5 shows two sample PIV images taken on the large and small rotors. These vortices are not generally axisymmetric as measured in the PIV plane. This is due to both the orientation of the vortex with respect to the PIV plane and the asymmetric nature of the flow itself. Also, the cross-plane flow is not uniform across the PIV plane. However, the cross-plane vorticity field clearly shows that there are multiple distinct vortices with varying viscous core sizes and strengths. It is possible to reduce the in-plane vorticity distribution into a sum of discrete, two-dimensional Gaussian vortices with axes perpendicular to the PIV plane. These vortices have velocity, $u_\theta(r)$, vorticity, $\omega(r)$, and circulation, $\Gamma(r)$, distributions at a radius r given by:

$$u_\theta(r) = \frac{\Gamma_O}{2\pi r}\left(1 - e^{-\eta_1 (r/a)^2}\right) \tag{1}$$

$$\omega(r) = \frac{\Gamma_O}{\pi}\frac{\eta_1}{a^2} e^{-\eta_1 (r/a)^2} \tag{2}$$

$$\Gamma(r) = \Gamma_0 (1 - e^{-\eta_1 (r/a)^2}) \tag{3}$$

where $\eta_1 = (1.121)^2 = 1.257$, and the maximum tangential velocity, u_C, occurs at the core radius, a, and is given by

$$u_C = \eta_2 \frac{\Gamma_O}{2\pi a} \tag{4}$$

with $\eta_2 = 0.715$. Integration of the radial momentum equation yields the pressure depression at the vortex centerline, $r = 0$,

$$\Delta P = p_C - p_\infty = -\eta_3 \rho_f \left(\frac{\Gamma_O}{2\pi a}\right)^2 \tag{5}$$

where $\eta_3 = 0.870$ (Oweis *et al.* (2003) [3]) and p_∞ is the pressure far from the vortex.

In reality, the flow also has vorticity with components parallel to the PIV plane as well as flow non-uniformity in the cross-plane flow. However, a combination of Gaussian vortices can be used to both re-construct the actual in-plane flow and scale the resulting vortex-induced pressure variations. Two parameters are needed to characterize each vortex: the core radius, a_i, and the total circulation $\Gamma_{O,i}$. Hereafter, the subscript, *i*, identifies the vortex in question, where *i* = 1 is the largest or "primary" vortex, and the remaining identified vortices are "secondary".

An identification procedure was used to find and fit Gaussian vortices to the regions of concentrated vorticity in each PIV image. A detailed description of the identification process is found in Oweis and Ceccio (2003) [4]. The identification is performed with the vorticity field, where concentrations of vorticity are used to identify the presence of a concentrated vortex, and gradients of the circulation are used to determine core size and consequently the strength of the identified vortex. Once the vortices are identified, the vorticity and velocity fields are then reconstructed and compared with the original measured fields. A regression value for the velocity field, R_V^2, and for the vorticity field, R_ω^2, were computed for each PIV image:

$$R_V{}^2 = \frac{\sum_{i=1}^{j} (V_{M,i} - V_{C,i})^2}{\sum_{i=1}^{j} (V_{M,i} - \overline{V}_M)^2} \tag{6}$$

$$R_\omega{}^2 = \frac{\sum_{i=1}^{j} (\omega_{M,i} - \omega_{C,i})^2}{\sum_{i=1}^{j} (\omega_{M,i} - \overline{\omega}_M)^2} \tag{7}$$

where subscripts *M* and *C* denote the measured and the computed (reconstructed) fields for the total number of PIV vector locations, *j*. Table 3 presents the average values of and for the data presented here. The values are averaged over all realizations at various downstream locations, *s/c*. A correlation value of 100 % signifies a perfect fit.

THE AVERAGED TIP-LEAKAGE FLOW FIELD

Multiple PIV images were collected for a given downstream position *s/c*. Between 501 and 586 images were collected at multiple downstream locations. Figure 6 shows the averaged flow fields for the two conditions of the small rotor (Re = 0.7 x 10^6 and 4.3 x 10^6) and two conditions of the large rotor (Re = 5.8 x 10^6 and 9.2 x 10^6) for varying downstream locations *s/c*. Note that the values of *s/c* chosen are similar but not identical for the five values of *s/c* shown. The closed contours are the outlines of the primary and secondary identified vortices.

	Reynolds Number	R_ω^2	R_V^2
5407 Rotor	0.7 x 10^6	72 +/- 10	65 +/- 12
"Small Rotor"	1.4 x 10^6	75 +/- 10	70 +/- 12
	2.8 x 10^6	75 +/- 9	68 +/- 9
	4.3 x 10^6	74 +/- 9	67 +/- 12
5206 Rotor	4.6 x 10^6	80 +/- 7	79 +/- 7
"Big Rotor"	5.8 x 10^6	77 +/- 9	76 +/- 9
	6.9 x 10^6	80 +/- 8	75 +/- 8
	8.1 x 10^6	77 +/- 9	75 +/- 10
	9.2 x 10^6	79 +/- 8	76 +/- 9

Table 3: Average correlation coefficients R_V^2 and R_ω^2 for the all measured conditions, *s/c*.

Interpretation of the average flow field must be performed with care, since vortex variability and wandering are significant. Moreover, multiple secondary vortices identified in the individual flow fields are not generally correlated in space with the primary vortex. Figure 7 shows the average number of identified vortices with varying downstream distance. The typical number is between 5 and 8, but the averaging of multiple images will smear out those vortices that are not approximately fixed in location. As a result, fewer vortices are discernable in the averaged flow field, with only one vortex identifiable farther downstream. For these reasons, the vortex identified in the average flow field is not equivalent to the typical vortex identified in the instantaneous flow fields. Oweis and Ceccio (2003) [4] provide an extended discussion of this issue. Consequently, we will present quantities identified from the instantaneous images of the flow field.

PROPERTIES OF THE INSTANTANEOUS TIP-LEAKAGE FLOW FIELD

The average value of the circulation identified in the primary vortex (solid line) and the total circulation identified (dashed line) are plotted for varying downstream distance in Figure 8. The average values of $\Gamma_{O,1}/(U_\infty R_P)$ and $\sum_i \Gamma_{O,i}/(U_\infty R_P)$ lie in a band. The strength of the primary vortex is approximately one-third to one-half that of the total identified strength. The strengths of the primary vortex reach a maxima near *s/c* = 0.13. For both quantities, the normalized values from the small rotor are less than those from the large rotor, and this is more pronounced for the strength of the primary vortex. However, there is no strong trend with Reynolds number. The case of **Re** = 4.6 x 10^6 (250 RPM on the large rotor) is anomalous.

These values can be compared to the average circulation in the rotor wake measured with LDV, shown in Figure 9. Here, the circulation is given by

$$G = \frac{1}{Z}\frac{r}{R}\frac{U_T}{U_\infty} \cong \frac{\Gamma}{2\pi R_P U_\infty} \tag{8}$$

where Z = 3 is the number of blades. Over most of the blade span, the circulation matches well for the two rotors. Past r/R_P = 0.95, however, the circulation is higher on the small rotor than on the large rotor due to the thicker duct boundary layer. Since the lift produced by the blade is the product of the circulation and the velocity, the total lift produced at the tip is closer in the two rotors than the plot of circulation would indicate. The maximum value of $2\pi G = \Gamma/U_\infty R_P \approx 0.4$ near r/R_P = 0.85, and this is similar to the maximum total value of identified circulation.

Farrell and Billet (1994) [2] examined the effect of tip clearance on the shed circulation downstream of the blade tip. They used LDV to determine the circulation of the primary vortex identified in the average field. The shed circulation was between 40% and 80% of the average bound circulation near the tip for clearance ratios from g/R_P = 0.004 to 0.024. The shed circulation increased with increasing g/R_P (The inlet boundary layer profile on the duct was not reported.) In the present flow, g/R_P = 0.015. Note that the circulation of the primary vortex is about 30% to 40% of bound circulation near the tip. This compares to a value of approximately 40% measured by Farrell and Billet (1994) for a flow of the same ratio of gap thickness to maximum blade thickness. Gopalan *et al.* (2002) [5] examined the strength of a tip-leakage vortex forming at the tip of a stationary hydrofoil, for g/t = 0.12, 0.28, and 0.52 (representing 22%, 52%, and 96% of the inlet boundary layer thickness). In these observations, however, the circulation of the leakage vortex was observed to decrease with increasing gap thickness. The reported lift coefficient near the tip was 0.48, implying a bound circulation of $\Gamma/U_\infty c \approx \frac{1}{2}C_L$ = 0.24. The average instantaneous shed circulation of the primary vortex was = 0.076, 0.061, and 0.046, or approximately 32%, 25%, and 19% of the bound vorticity near the tip.

The average core radius of the primary vortex is plotted in Figure 10. There are discernable differences between the radii measured downstream of the large and small rotors, with the normalized core radius of downstream of the large rotor tips approximately 20% larger than those from the smaller rotor. Considering each rotor separately, increases in Reynolds number leads to a decrease in average core size, although the dependence is not strong. Again, the case of **Re** = 4.6 x 10^6 (250 RPM on the large rotor) is anomalous, with the trend in core size with *s/c* opposite that of the trends identified for all the other conditions. The core radius of the larges vortex is comparable to the normalized tip clearance, = 0.015 (g/t = 0.17). Reynolds number scaling of the free tip-vortices often follows the analysis of McCormick (1962) [6], where the core size is related to the boundary layer thickness at the trailing edge of the lifting surface. Chesnakas and Jessup (2003) [1] report that the blade wake displacement thickness, δ_1/R_P, at r/R_P = 0.99 was 0.0121 for **Re** = 1.4 x 10^6 and 2.8 x 10^6, and 0.0073 for **Re** = 4.3 x 10^6 for the small rotor, and 0.0070 at **Re** = 9.2 x 10^6 for the large rotor. The variation of the wake thickness with Reynolds number (a reduction of about 60%) in is not paralleled

by equivalent changes in the core radius of the primary vortex (a reduction of approximately 6%) for the small rotor. The general differences in the average core size between the large and small rotors may have resulted from the differences of the shroud inlet boundary layer, as discussed above. Farrell and Billet (1994) [2] examined the relationship between the core-size identified on the average flow field as a function of tip clearance. They found that the core radius *a/t* was much larger than the gap clearance *g/t*, for cases of smaller gap clearances, even after correction for vortex wandering was applied. This was surprising, since it is expected that the vortex core size should scale with the clearance. Here, the variation in the core radii identified on the individual images do not vary widely with Reynolds number and are on the order of twice the gap clearance. Gopalan *et al.* (2002) [6] report core radii on the order of a/c = 0.006 +/- 0.001 (a/t = 0.06 +/- 0.01) (where c = 0.050 m was the foil chord, which was also equal to the span, and t = 0.005 m was maximum thickness at the tip). While the resolution of these measurements was limited, the normalized core radii are smaller than those reported here, and were observed to be approximately constant with varying gap size. In the present study, the average values of a_1/t vary from 0.12 to 0.16.

Figure 11 shows the evolution of the pressure coefficient, $C_{P,1} = \Delta P_1 / \frac{1}{2}\rho U_\infty^2$, of the primary vortex with downstream location. The pressure is computed using equation 5. While the true pressure in the location of the vortex cores is affected by the presence of the surrounding vortices and the three-dimensionality of the flow, the pressure computed here scales the pressure depression due to the local concentration of vorticity. The lowest pressure reduction in the primary vortex core occurs for 0.05< s/c < 0.15. The pressure inside the core begins to increase after this downstream location. The inferred pressures are lower in general for the large rotor, and the trend with Reynolds number is weak.

VARIABILITY OF THE INSTANTANEOUS TIP-LEAKAGE FLOW FIELD

Significant variability exists between different instantaneous realizations of the flow. Figures 12, 13, and 14 present histograms of the quantities $\Gamma_{O,1}/U_\infty R_P$, a_1/R_P, and $C_{P,1}$ all for the strongest identified vortex. Also plotted are vertical lines delineating the average of the quantity identified in each image. The peak values are almost twice the average values for most distributions, and the shape of the distributions are only qualitatively similar to a normal distribution about a mean value. The typical standard deviation is between 27% and 50% of the mean value for $\Gamma_{O,1}/U_\infty R_P$, between 17% and 25% for a_1/R_P, and between 28% and 54% for $C_{P,1}$. These values are slightly higher than the standard deviations of 15% to 25% of the mean vortex strength reported by Gopalan *et al.* (2002) [5]. The distributions for each rotor are comparable, but there are some differences between the histograms when comparing between the two rotors, especially for the histograms of $\Gamma_{O,1}/U_\infty R_P$. There is a discernable correlation between the vortex strength and core size, as indicted in Figure 15. This suggests that the maximum tangential velocity of the vortices is relatively constant for a given rotation rate of the rotor.

Figures 16 and 17 plots the positions of the identified primary and secondary vortices. All of the primary vortices have the same direction of rotation, while a fraction of secondary vortices are counter-rotating with respect to the primary vortex. In the case of the small rotor, the primary vortex is sometimes identified in the wake spiral rather than in the position of the tip-leakage vortex. This illustrates that the circulation of the strongest secondary vortex often approaches that of the primary vortex. This is much less common for the large rotor. The loci of vortex positions near the trailing edge map out the wake spiral, and the region of highest vortex probability near the rotor trailing edge. The patterns are qualitatively similar between the small and large rotors. However, the secondary vortices in the wake spiral of the large rotor are somewhat more spatially correlated with the primary vortex, as evidenced by the stronger clustering of the secondary vortices.

The axis of the primary vortex is observed to wander in a cluster around the mean position. The amplitude of the wandering increases with increasing s/c. Near the tailing edge, the standard deviation of the distance of the vortex from the mean location, κ, varies from κ/a = 0.97 near the trailing edge of the small rotor to 1.12 at the farthest downstream location. For the large rotor, κ/a = 0.57 near the trailing edge and 1.06 at the farthest downstream location investigated. These values are significantly lower than an approximate value of κ/a > 3 measured by Gopalan *et al.* (2002) [5].

DIRECT AND SCALED VELOCITY FLUCTUATION

The average flow fields were calculated and subtracted from the mean squared fields to compute velocity fluctuations. The PIV velocity measurements in this study resolved on the order of ten velocity measurements across the diameter of the primary vortex, and these measurements were spatially averaged with the overlap of the PIV interrogation windows. Consequently, we do not expect to resolve the smallest scales of velocity fluctuations in the vortical flow. In order to understand the effect of vortex wandering, variable vortex strength, and the presence of multiple vortices, the individual flow fields can be shifted and scaled to reduce these effects, as discussed in Oweis and Ceccio (2003) [4]. The effect of primary vortex wandering can be reduced by the in-plane shifting of the individual flow fields such that the axes of the primary vortices are aligned before averaging and the calculation of velocity fluctuations. However, the spatial shifting of the individual images does not account for the variability of the strength and core size of the individual primary vortices. This effect can be reduced by scaling each individual flow field with the identified circulation and core size, a_1 and $\Gamma_{O,1}$ derived from each individual realization.

Figure 18 shows the averaged vorticity fields after shifting and internally scaling each image for the four conditions of Figure 6. The vorticity is scaled by $\omega_C = \eta_2 \Gamma_{O,1} / \pi a_1^2$ and is

plotted in the normalized spatial coordinates $[(x/a_1),(y/a_1)]$. Comparison with Figure 6 indicates that the positions of the strongest secondary vortices are not spatially correlated with the center of the primary vortex. The cores of the averaged vortices shown in Figure 6 are ellipsoidal, suggesting that the vortex is undergoing an-isotropic wandering, as discussed in Oweis and Ceccio (2003).

Figures 19 and 20 show the velocity fluctuations $\left(\overline{u'}^2 + \overline{v'}^2\right)/U_{C,1}^2$ computed directly and after scaling and shifting for the small and large rotor. The velocity fluctuations are normalized by $U_{C,1} = \eta_2 \overline{\Gamma_{O,1}}/(2\pi \overline{a_1})$, where the maximum tangential velocity of the primary vortex based on the circulation and core size derived from the averaged flow field. Large velocity fluctuations are seen near the cores of the un-scaled vortices, with magnitudes of ~ 0.2. The velocity fields were shifted and normalized, and the velocity fluctuations were computed and normalized with $\eta_2 \overline{\Gamma_{O,1}}/(2\pi \overline{a_1}) = 0.114$. The resulting fluctuations $((ua_1/\eta_2\Gamma_{O,1})')^2 + ((va_1/\eta_2\Gamma_{O,1})')^2$ are plotted in the normalized spatial coordinates $[(x/a_1),(y/a_1)]$. The residual fluctuations near the primary vortex axis increase, with the largest increases occurring downstream. The process of shifting and scaling has revealed how the presence of the uncorrelated secondary vortices can lead to relatively large velocity variability. This phenomenon becomes more pronounced as the Reynolds number for each rotor increases. It is interesting to note that the scaled variability increase with increasing downstream distance from the point of maximum average vortex strength.

It is worth mentioning that scaling the instantaneous velocity fields with the instantaneous summed circulation of the identified vortices and the core size of the primary vortex (not shown here) produced similar trends to the results discussed above. Significant increase in the velocity fluctuation with increasing s/c was noticed. However, it is more appropriate to use the circulation and core size of the instantaneous primary vortex for scaling, than the summed circulation.

VORTEX PROPERITES AND CAVITATION INCEPTION

The inception characteristics of the two rotors was reported in Chesnakas and Jessup (2003) [1]. Inception was called when an average of one cavitation event per second was detected acoustically after a drop in free-stream pressure. Figure 21 shows the cavitation inception number, $\sigma_i = (P_\infty - P_V)/\frac{1}{2}\rho U_\infty^2$, as a function of Reynolds number for both rotor configurations. The inception occurs at increasing cavitation numbers with increasing Reynolds number, and the values range from $9 < \sigma_i < 12$ for 2 x 10^6 < **Re** < 1 x 10^7.

A high-speed video camera with a post-trigger delay was used to capture images of the small cavitation bubbles. The bubbles first occurred at *s/c* ~ 0.5. They were small, with dimensions typically on the order of millimeters, and they were not generally spherical, but often were oblong and sometimes in shape of small spirals.

The observed pressure and location of inception can be compared with the inferred pressures of the primary vortex. Examination of Figure 11 indicates that the primary vortex has a minimum pressure at *s/c* ~ 0.1, with a pressure coefficient -4.5 < $C_{P,1}$ < -6.5. As *s/c* ~ 0.5, the observed location of inception, the pressure coefficient ranges from -2 < $C_{P,1}$ < -3. The pressure in the vortex reached vapor pressure when $C_{P,1} = -\sigma_i$. Consequently, inception is occurring when the pressure in the core of the primary vortex is about *four times* higher than vapor pressure. The histograms of pressure coefficient shown in Figure 14 indicate that the minimum observed pressure coefficients at this location ($C_{P,1}$ ~ -5) are still much higher than those needed to cause cavitation. However, inception is observed to occur in the region of increased relative flow variability, as seen in Figures 19 and 20. It is important to mention that the axial velocity in the vortex core can change the inferred pressure coefficients only slightly, and most of the pressure drop at the vortex axis is due to the rotational motion.

The size of the bubbles is much smaller than the size of the primary vortex core at the location of inception. The core size varied from 0.010 < a_1/R_P < 0.015, implying a core diameter on of ~10 mm for the large rotor. The bubbles observed had dimensions that were on typically 1/10th the core dimensions.

CONCLUSIONS

The data presented above indicate that the strength and core size of the vortices are weakly dependant on Reynolds number, but are affected by variation in the inflowing duct boundary layer. The total circulation identified in the wake of the tip region is approximately 40% of the bound circulation near the tip, but the circulation of the largest vortex associated with the tip-leakage flow is about 1/3 of the total. Distinct vortices can be identified as far *s/c* = 0.7. The core sizes of the tip-leakage vortices do not vary strongly with varying boundary layer thickness on the blades or the duct. Instead, its typical dimensions are on the order of the tip clearance.

There is significant flow variability for all Reynolds numbers and rotor configurations. Scaled velocity fluctuations near the axis of the primary vortices show significant increases in with downstream distance, suggesting the presence of spatially uncorrelated secondary vortices and the possible existence of three-dimensional vortex-vortex interactions. These changes in relative flow variability are not apparent in the un-scaled average flow fields. It is only after shifting and scaling that these flow features become apparent.

The tip-leakage vortex does not smoothly merge with the co-rotating secondary vortices. Instead, a series of distinct vortices orbit and redistribute in space with increasing *s/c*. It is possible that complex vortex interactions are taking place between the primary and secondary vortices. Such a three-dimensional vortex interactions have been observed by Savas and co-workers (Chen *et al.,* (1999) [7] and Ortega *et al.* (2003) [8]). They have shown how both co- and counter-rotating vortices of unequal strength can undergo an instability that results in the wrapping of the weaker vortex around the stronger

one. The onset of this wrapping can occur relatively far downstream of the position of the vortices' formation. When the secondary vortex is captured by the rotational flow of the primary vortex, the unsteadiness of the flow field significantly increases. The significant increase in the relative flow variability downstream near may therefore result from such complex vortex-vortex interactions. However, resolution of such a complex flow is not possible with the planar PIV system used here. However, the observations of inception suggest that such vortex interactions may be occurring. This would account for the increased variability in the flow at the location of vortex inception, the observation of inception at such high average pressures, and the size and shape of the observed bubbles. Stretching of secondary vorticity in jets and shear layers has been identified as a primary source of cavitation inception (see, for example, Ran and Katz (1994) [9] and Iyer and Ceccio (2002) [10]). It is likely that a similar mechanism is at work in the present flow.

ACKNOWLEDGMENTS

This work was performed under the joint sponsorship of the NAVSEA 93R propulsor program and the Office of Naval Research 6.2 propulsor program. Support for the University of Michigan was under ONR grant number N00014-99-1-0307, Dr. Ki-Han Kim technical monitor.

REFERENCES

[1] Chesnakas, C., and Jessup, S. 2003, "Tip vortex induced cavitation on a ducted propulsor," *Proc. 4th ASME-JSME Joint Fluids Engineering Conference*, FEDSM2003-45320, Honolulu, Hawaii.

[2] Farrell, K. J. and Billet, M. L. 1994, "A correlation of Leakage vortex cavitation in axial-flow pumps," *J. Fluids Engineering*, 116, 551-557.

[3] Oweis, G.F., Choi, J., Ceccio, S.L., 2003, "Dynamics and noise emissions of laser induced bubbles in a vortical flow field," *J. Acoustical. Society of America* (accepted)

[4] Oweis, G. F. and Ceccio, S. L. 2003, "Instantaneous and Time Averaged Flow Fields of Multiple Vortices in the Tip Region of a Ducted Propulsor," *Experiments in Fluids*, (submitted).

[5] Gopalan, S., Katz, J., and Liu, H. L. 2002, "Effect of gap size on tip leakage cavitation inception, associated noise, and flow structure," *J. Fluid Eng.*, **124**, 4, 994-1004.

[6] McCormick, B. W. 1962, "On cavitation produced by a vortex trailing from a lifting surface," *Trans. ASME, Journal of Basic Engineering*, **84,** Series D, No. 3, 369-379,

[7] Chen, A.L., Jacob, J.D. and Savaş, Ö. 1998, "Dynamics of co-rotating vortex pairs in the wakes of flapped airfoils," *J. Fluid Mechanics*, **382**, 155-193

[8] Ortega, J. M., Bristol, R. L., and Savaş, Ö. 2003, "Experimental study of the instability of unequal-strength counter-rotating vortex pairs," *J. Fluid Mech.*, **474**, 35-84.

[9] Ran, B., and Katz, J., 1994, "Pressure Fluctuations and Their Effect on Cavitation Inception Within Water Jets," *Journal of Fluid Mechanics*, **262**, pp. 223-263.

[10] Iyer, C.O. and Ceccio, S.L. 2002, "the Influence of Developed Cavitation on the Flow of a Turbulent Shear Layer," *Physics of Fluids*, **14**(10), pp. 3414- 3431.

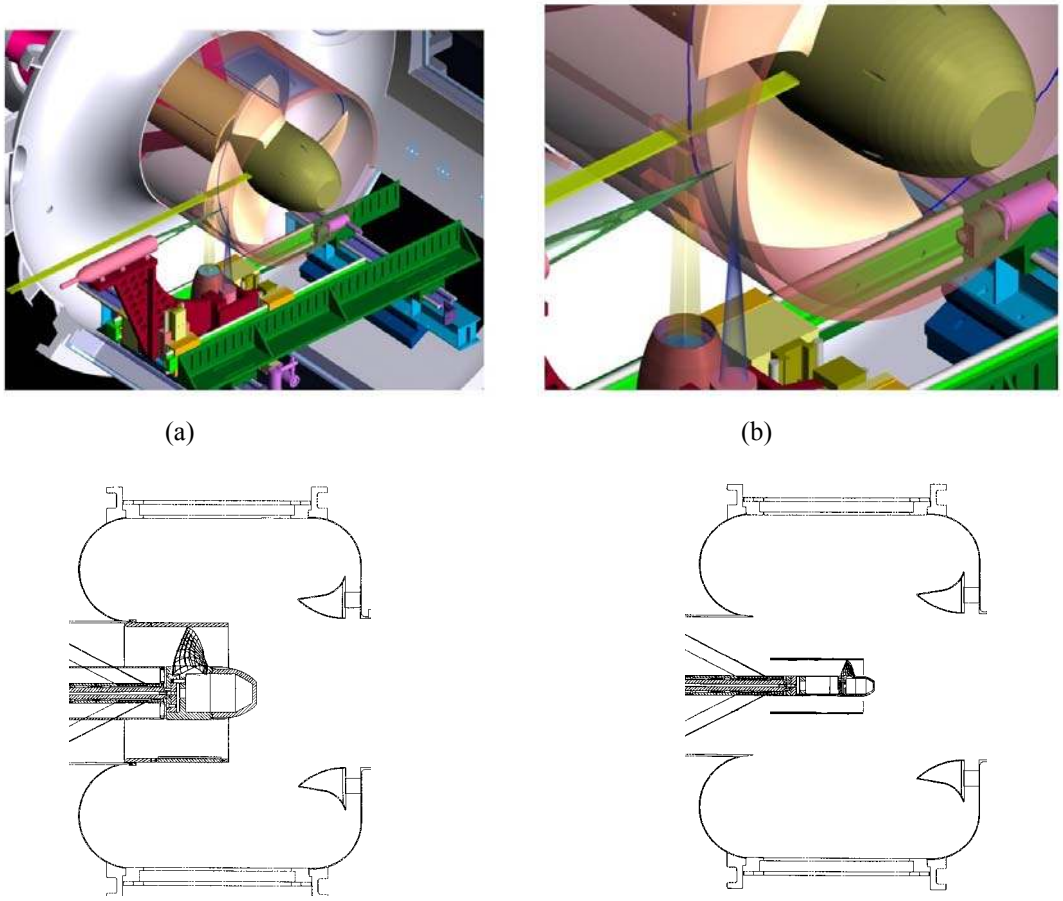

Figure 1: (a) A diagram of the open-jet test section of the Naval Surface Warfare Center 36-Inch Variable Pressure Cavitation Tunnel with the three-bladed, ducted rotor P5206 installed; **(b)** a close up view of the blade tip at the trailing edge (1), the emanating tip leakage vortex - the dark curved line (2), the camera housing (3), the laser light sheet passing through an insert in the duct (4), and the hub (5); **(c)** A diagram of the open-jet test section of the 36" diameter Water Tunnel, showing the P5206 propeller duct, which is an extension of the tunnel conduit; **(d)** Diagram of the open jet test section with the P5407 ducted propeller installed.

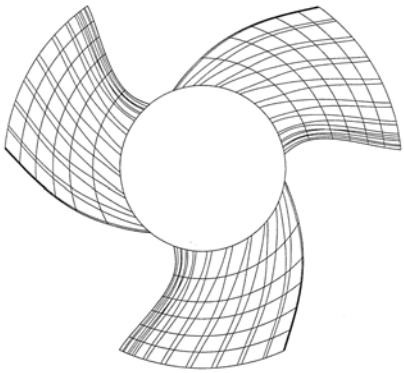

Figure 2: Plan view of the rotor.

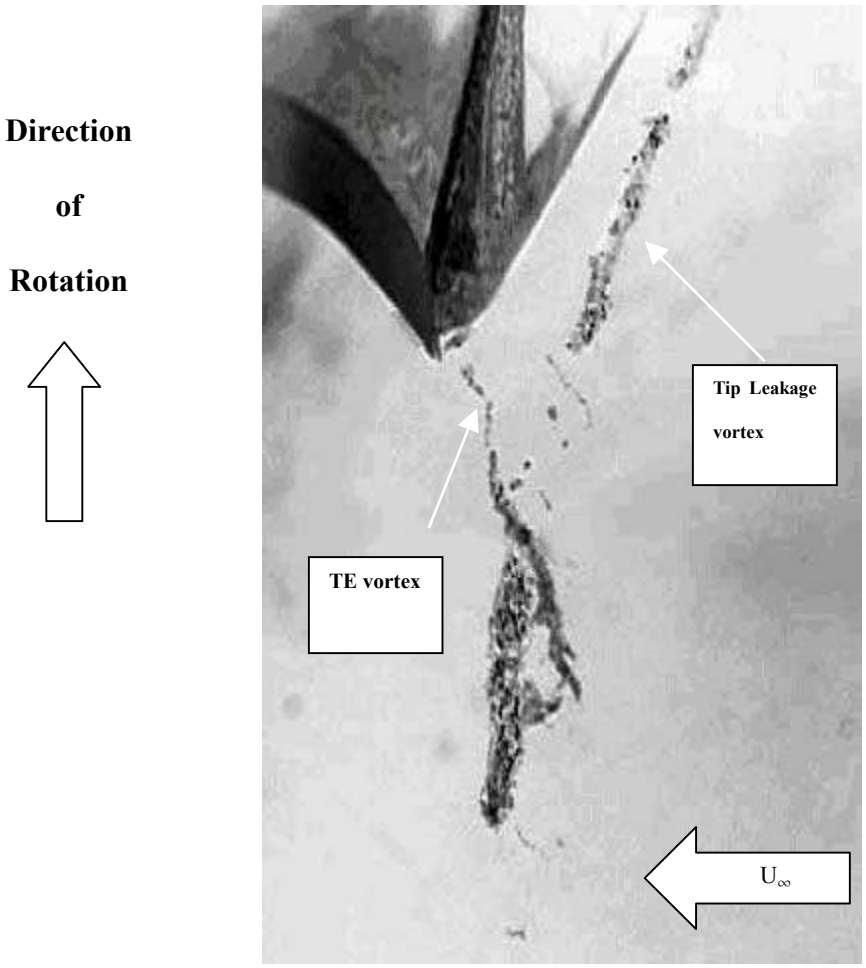

Figure 3: A photograph of the blade trailing edge taken through a clear section of the duct. The pressure has been lowered, and developed vortex cavitation visualizes the tip leakage and trailing edge (TE) vortices. The cavitation number is $\sigma = 5.6$.

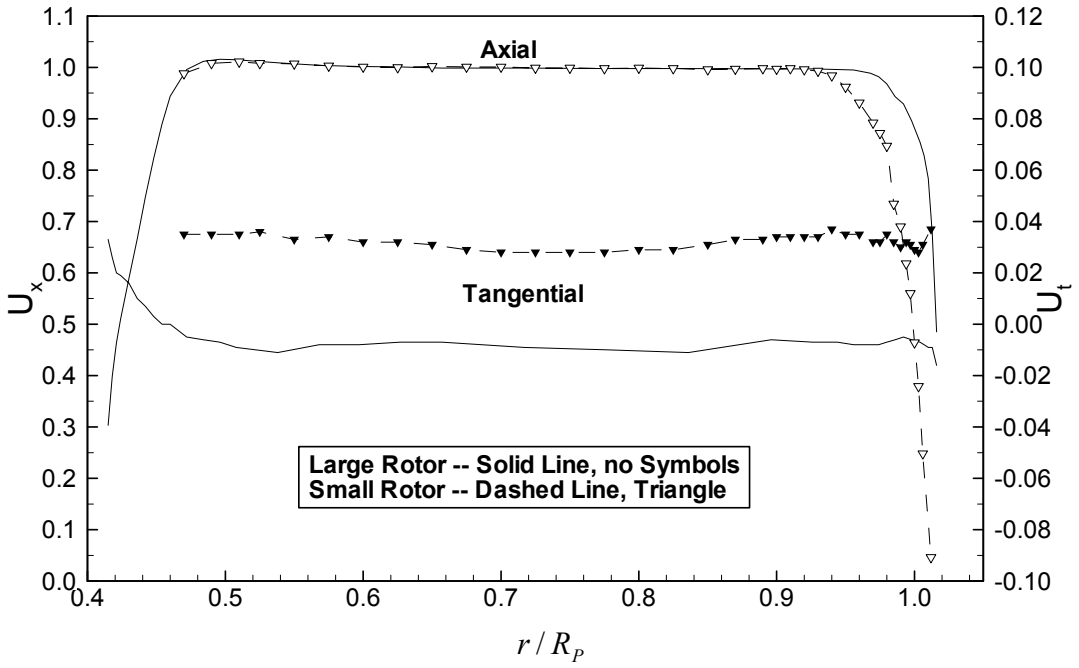

Figure 4: Tangential (U_t / U_∞), and axial (U_x / U_∞) velocity profiles of the duct inflow for the small rotor (triangles), and for the large rotor (solid line with no symbols). n = 1200 rpm for the small rotor, and 500 rpm for the large rotor.

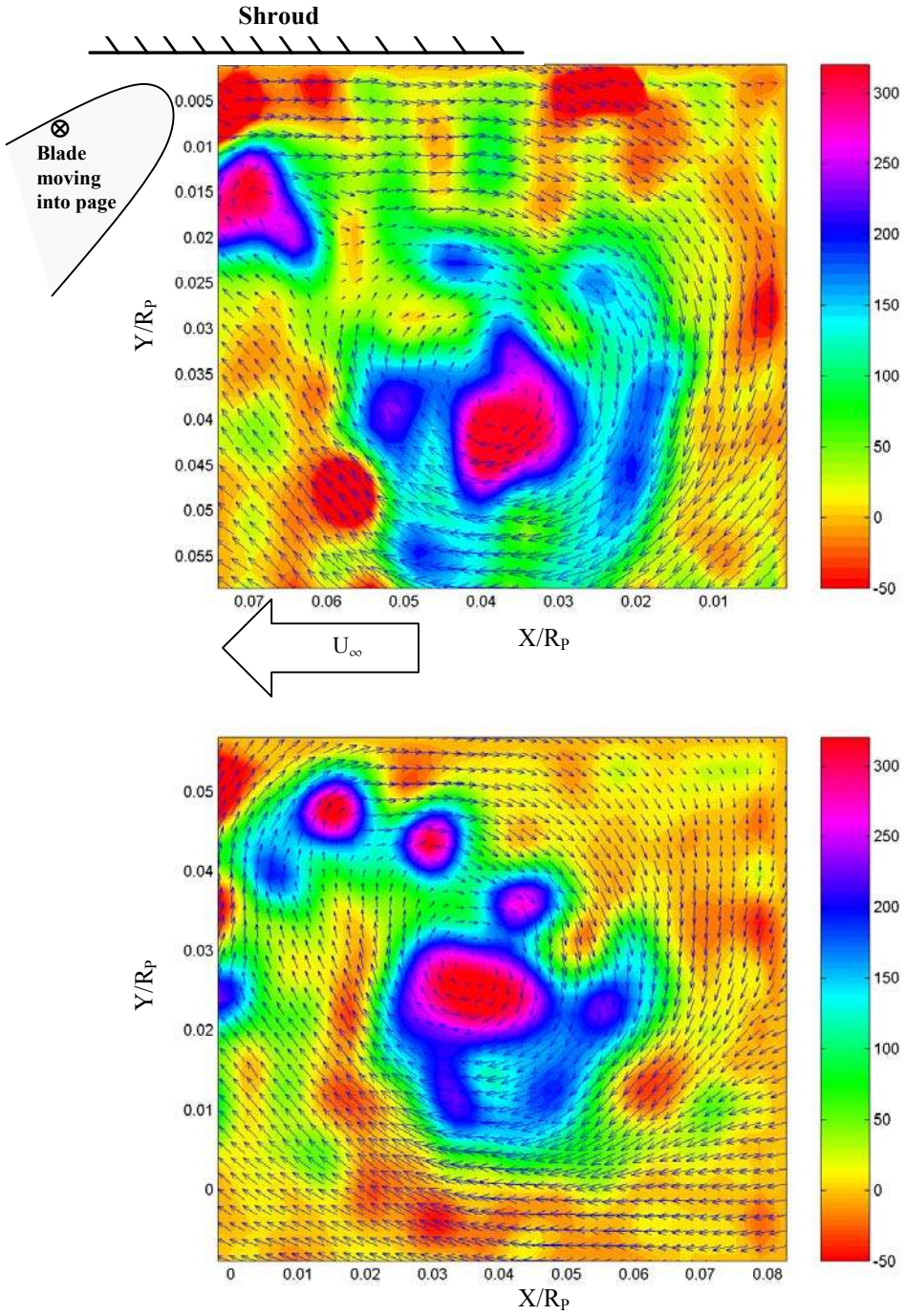

Figure 5: Sample instantaneous PIV velocity vector fields with vorticity contours from the mini rotor at 1200 RPM [Re = 2.8M] (top), and the big rotor at 438 RPM [Re = 8.1M] (bottom) at the downstream location $s/c = 0.041$. The vorticity is normalized by (U_∞ / R_P).

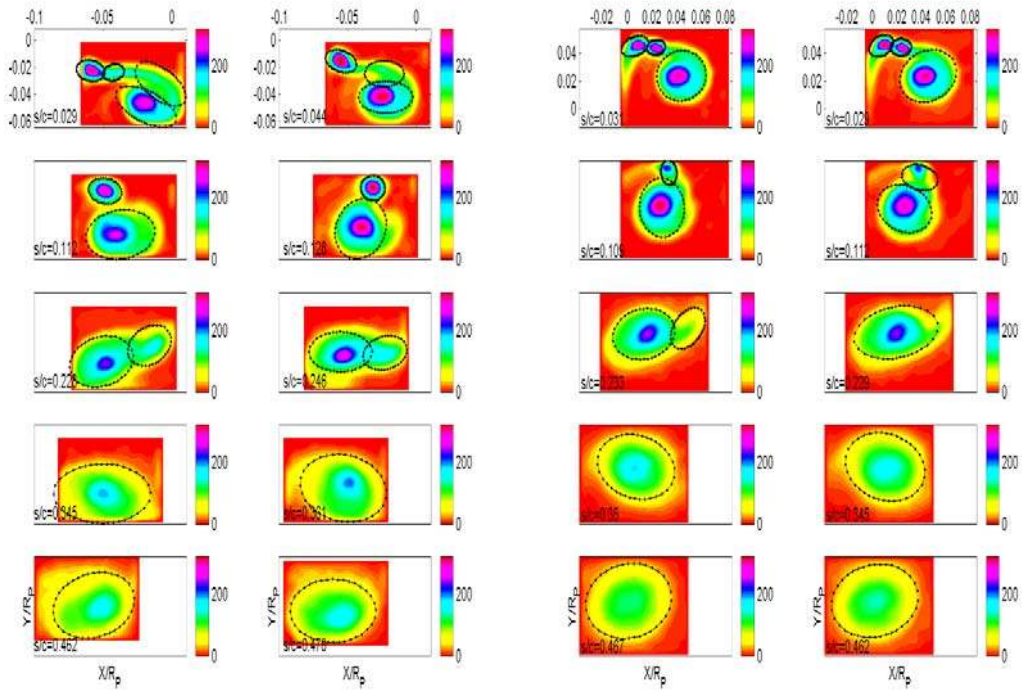

Figure 6: Average vorticity field development as a function of the distance downstream from the blade trailing edge along the pitch line, *s/c*. The small rotor (left) running at (a) 300 RPM [Re = 0.7M], and (b) 1800 RPM [Re = 4.3M]. The large rotor (right) running at (c) 313 RPM [Re = 5.8M], and (d) 500 RPM [Re = 9.2M]. The closed contours indicate the core limits of the identified vortices. The axes coordinates are normalized by R_P and the vorticity by (U_∞ / R_P).

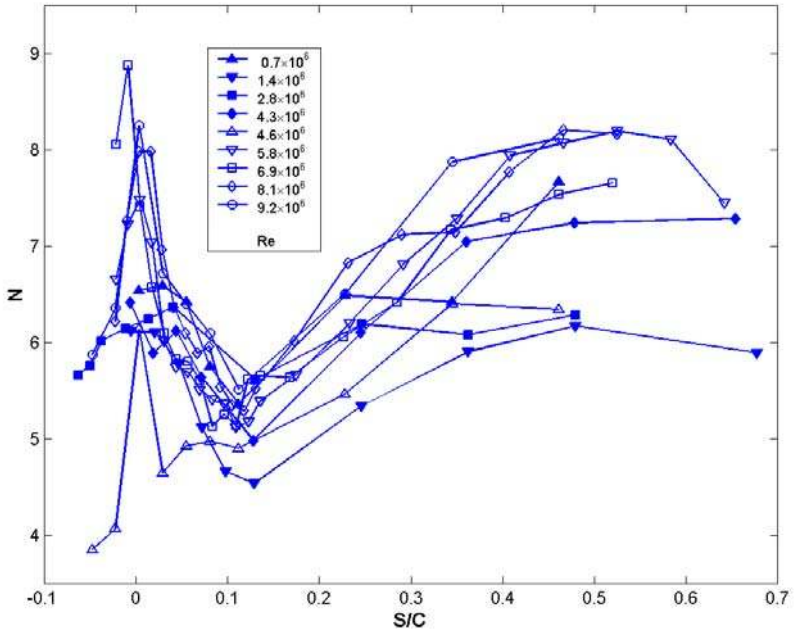

Figure 7: The average number of identified vortices identified, *N*, in the instantaneous field as a function of the distance downstream from the blade trailing edge along the pitch line, *s/c*. Closed symbols correspond to the small rotor, open symbols to the large rotor.

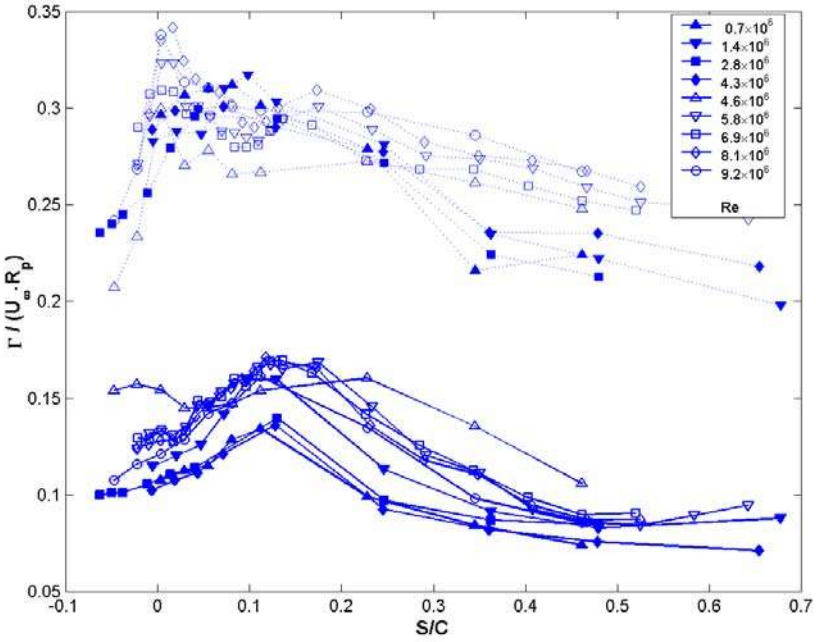

Figure 8: Average identified circulation of the primary vortex (solid line), and the average sum of the circulation of the identified vortices in the field (dashed line). Closed symbols correspond to the small rotor, open symbols to the large rotor.

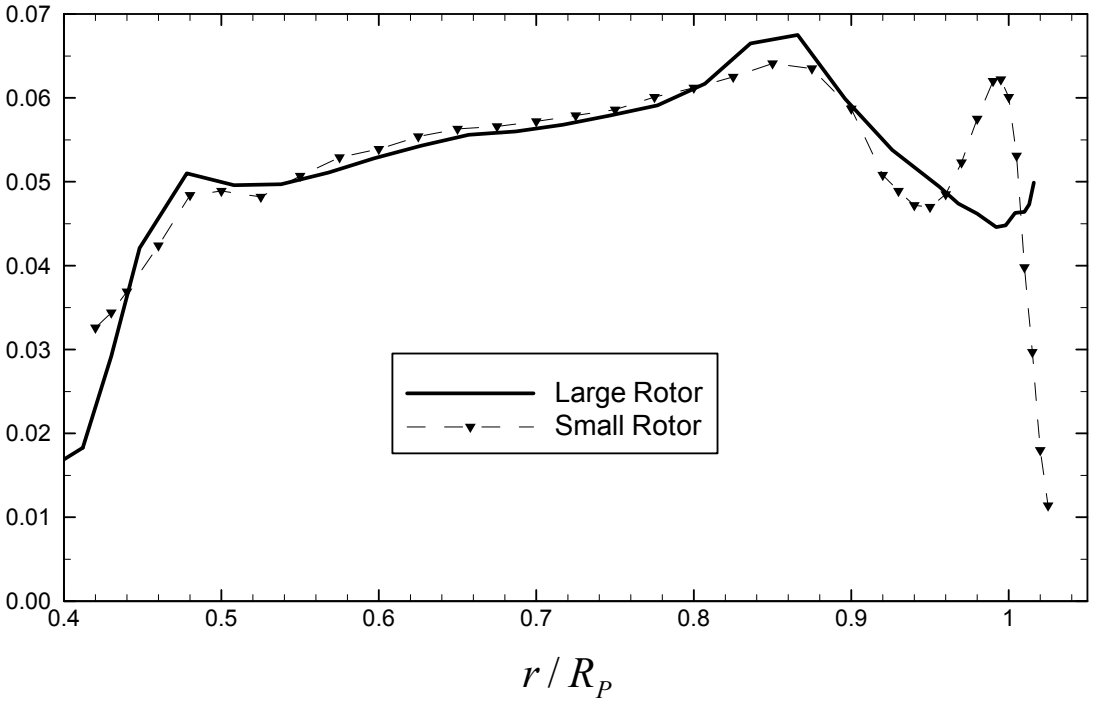

Figure 9: Circulation, G, measured downstream of the large and small rotors at $x/R_P = 0.650$.

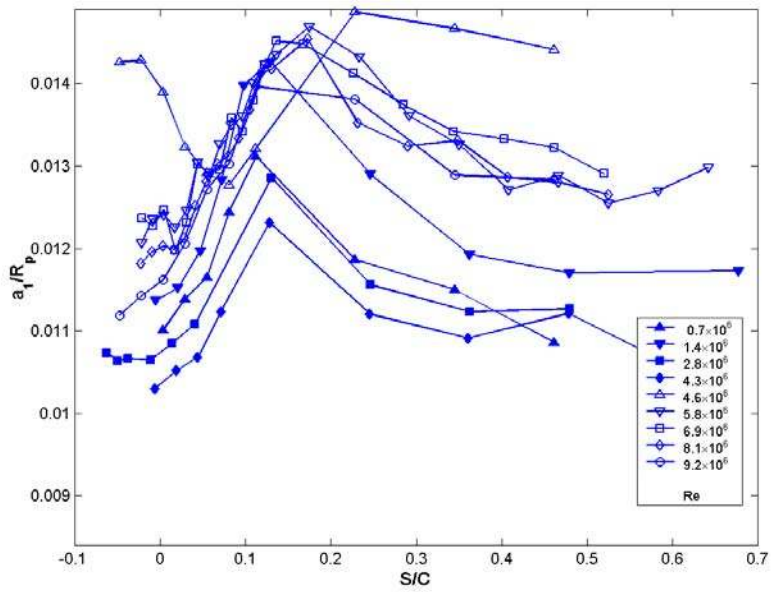

Figure 10: Average of the identified core radius of the primary identified vortex as a function of the downstream distance *s/c*. Closed symbols correspond to the small rotor, open symbols to the large rotor.

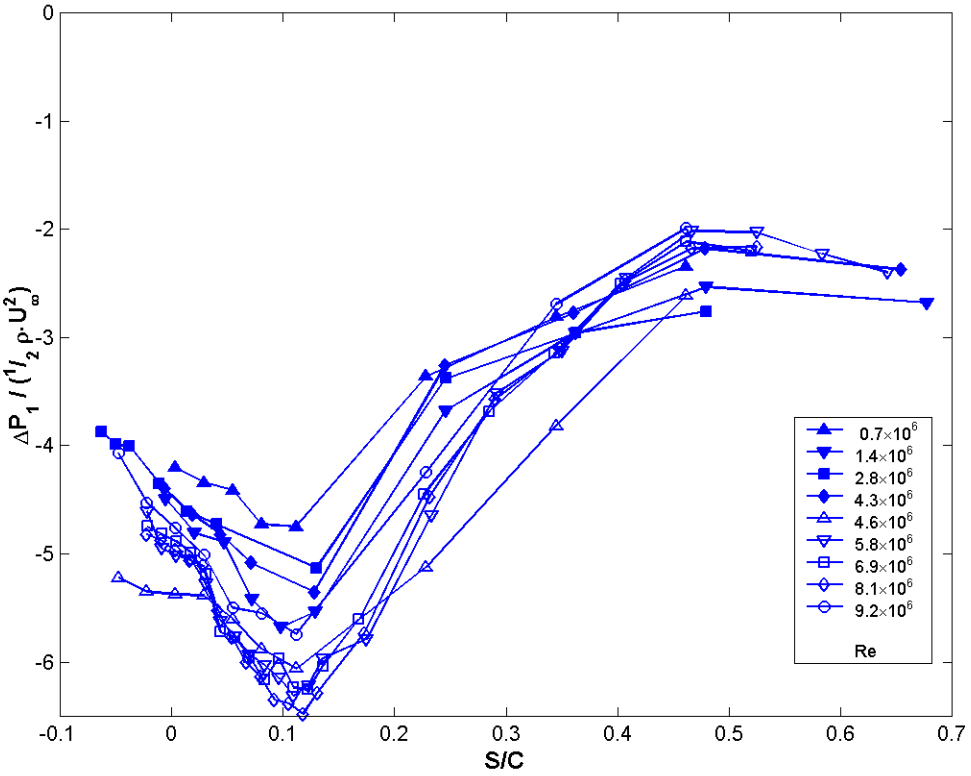

Figure 11: Average of the inferred pressure coefficient of the instantaneous primary vortex $C_{P,1} = \Delta P_1 / (\frac{1}{2}\rho U_\infty^2)$ as a function of *s/c* for varying Reynolds numbers. Closed symbols correspond to the small rotor, open symbols to the large rotor.

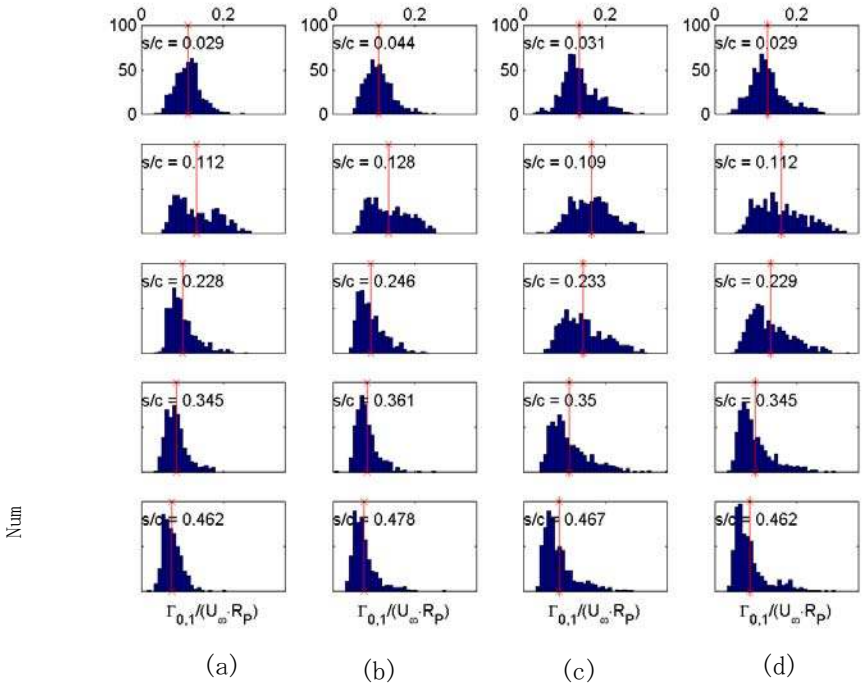

Figure 12: Histograms of the primary vortex circulation, $\Gamma_{O,1}/(U_\infty R_P)$, at varying downstream distance, *s/c*. The small rotor running at (a) 300 RPM [Re = 0.7M], and (b) 1800 RPM [Re = 4.3M]. The large rotor running at (c) 313 RPM [Re = 5.8M], and (d) 500 RPM [Re = 9.2M].

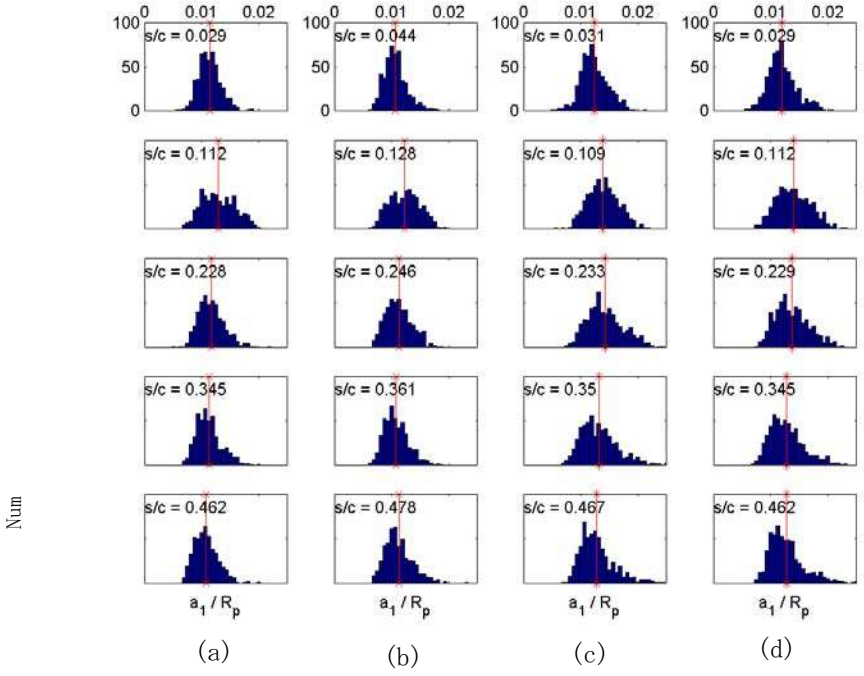

Figure 13: Histograms of the primary vortex core radius, a_1 / R_P. Conditions are the same as **Figure 12**.

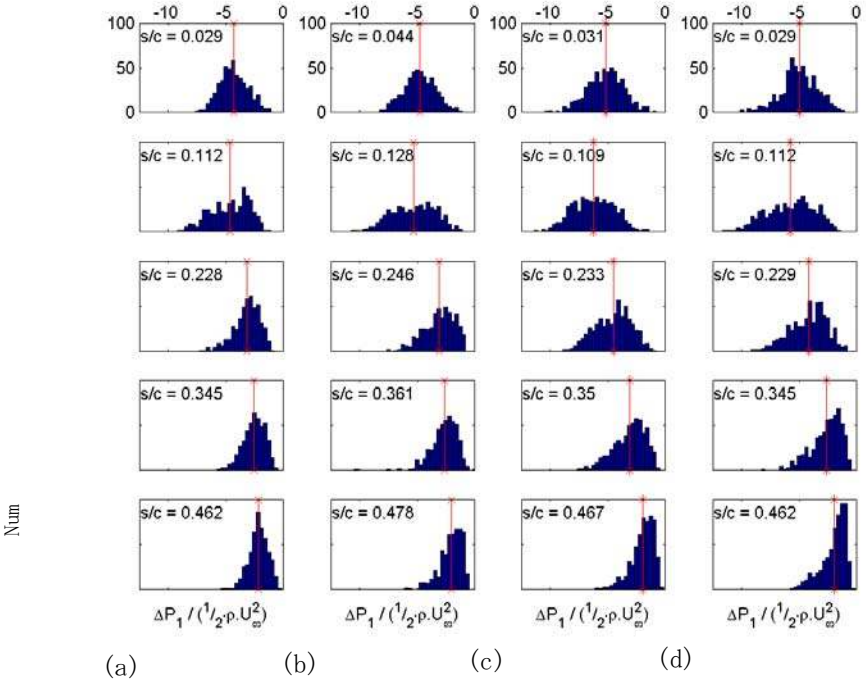

Figure 14: Histograms of the primary vortex pressure coefficient, $C_{P,1}$. Conditions are the same as **Figure 12**.

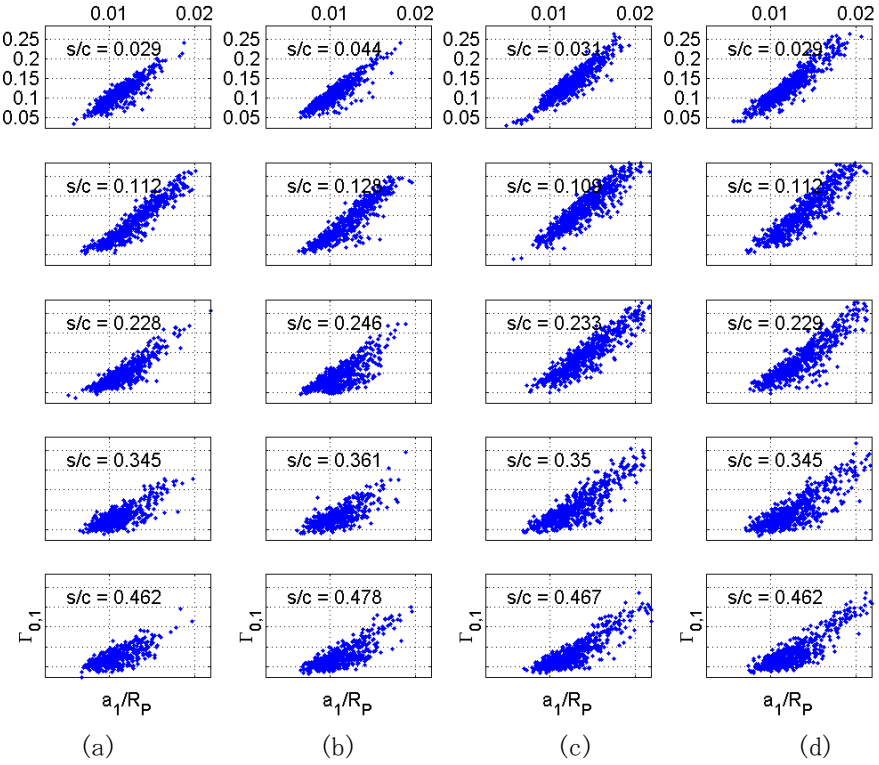

Figure 15: A plot of $\Gamma_{0,1}/(U_\infty R_P)$ versus a_1/R_P for the conditions shown in **Figure 12**.

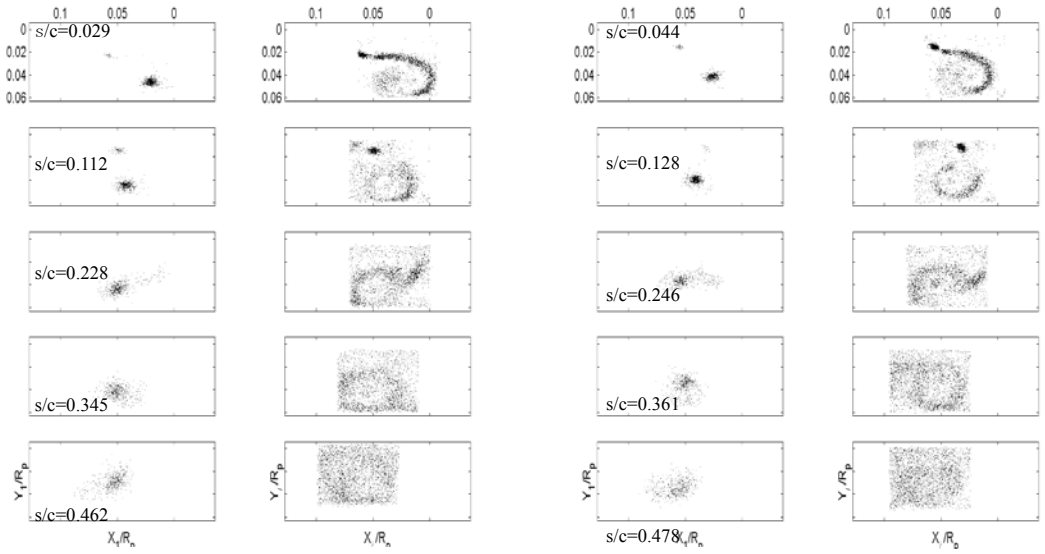

Figure 16: Scatter-plot of the center location of (a, c) the primary vortex (b, d) the secondary vortices at (i) 300 rpm [Re = 0.7M], and (ii) 1800 rpm [Re = 4.3M] for the small rotor conditions in **Figure 12**.

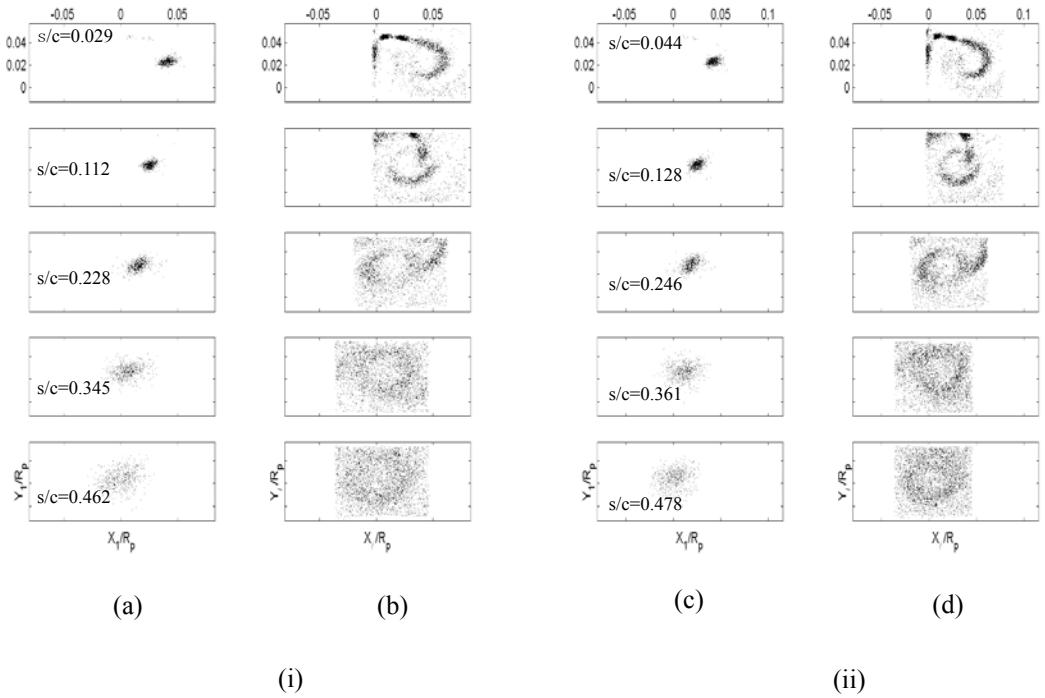

Figure 17: Scatter-plot of the center location of (a,c) the primary vortex (b,d) tne secondary vortices at (i) 313 rpm [Re = 5.8M], and (ii) 500 rpm [Re = 9.2M] for the large rotor conditions in **Figure 12**.

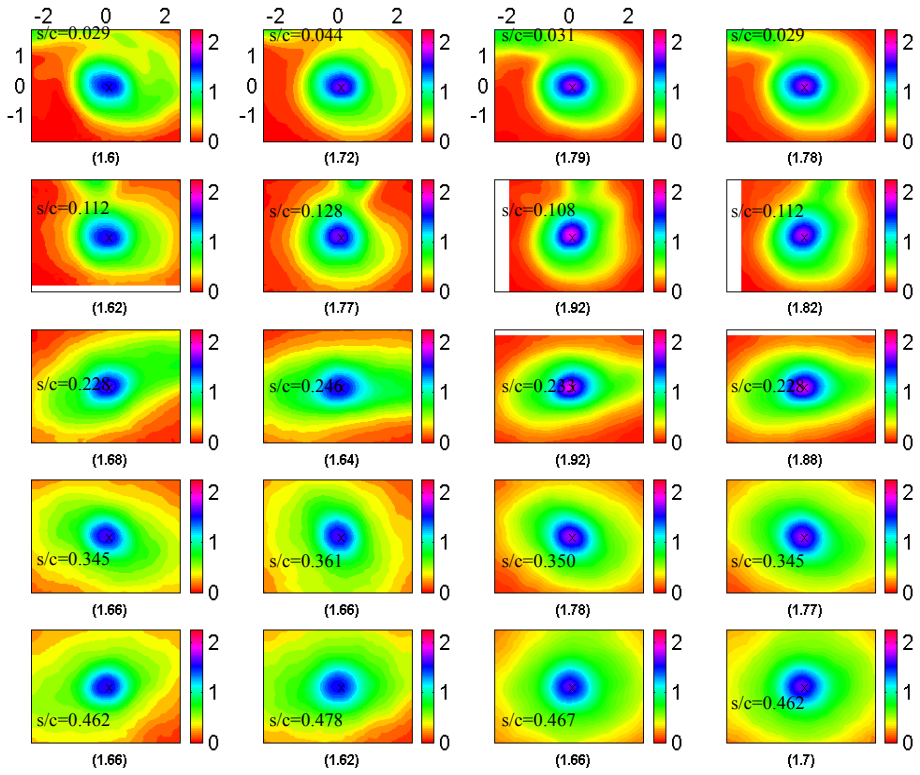

(a) (b) (c) (d)

Figure 18: Scaled and shifted vorticity ω contours for the small rotor: (a) Re=0.7M (300 rpm), (b) Re = 4.3M (1800 rpm); and for the large rotor (c) Re = 5.8M (313 rpm), and (d) Re= 9.2 (500 rpm). The value at the center of the primary vortex is also noted below each plot. The s/c value is noted on each plot.

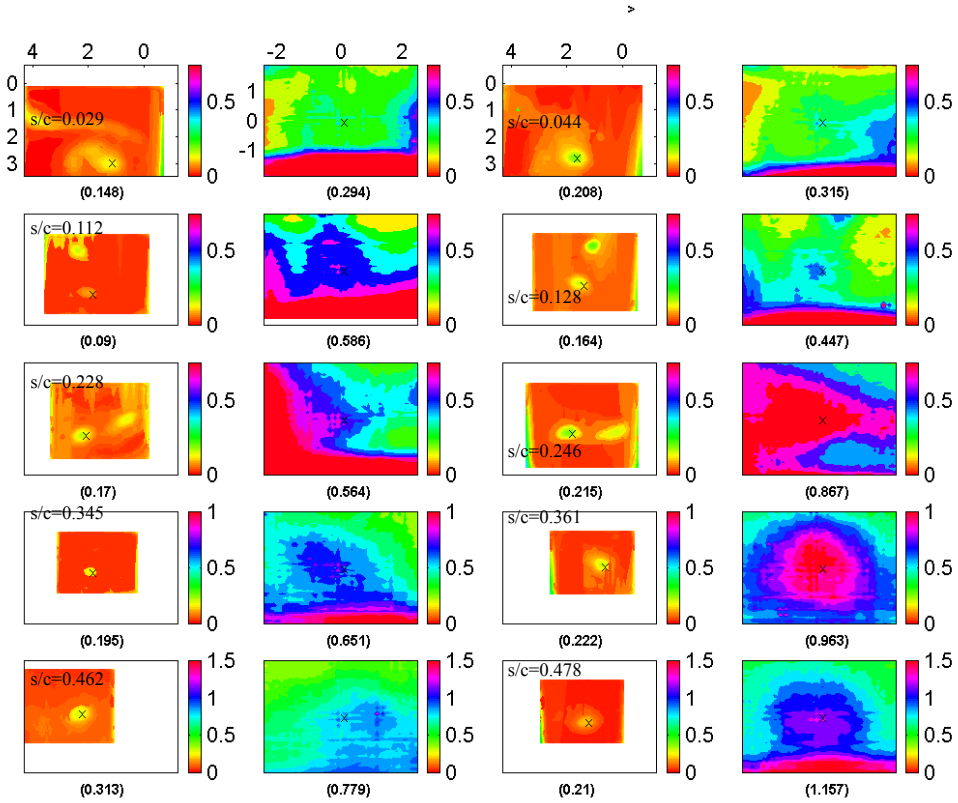

(a) (b) (c) (d)

Figure 19: Velocity fluctuations $\overline{u'^2} + \overline{v'^2}$ for the small rotor. (a, c) are the directly computed fluctuations, and (b, d) are the scaled fluctuations after scaling and shifting. (a, b) correspond to n = 300 rpm, while (b, d) correspond to n = 1800 rpm. The value at the center of the primary vortex is noted below each plot, and the downstream location s/c is prescribed.

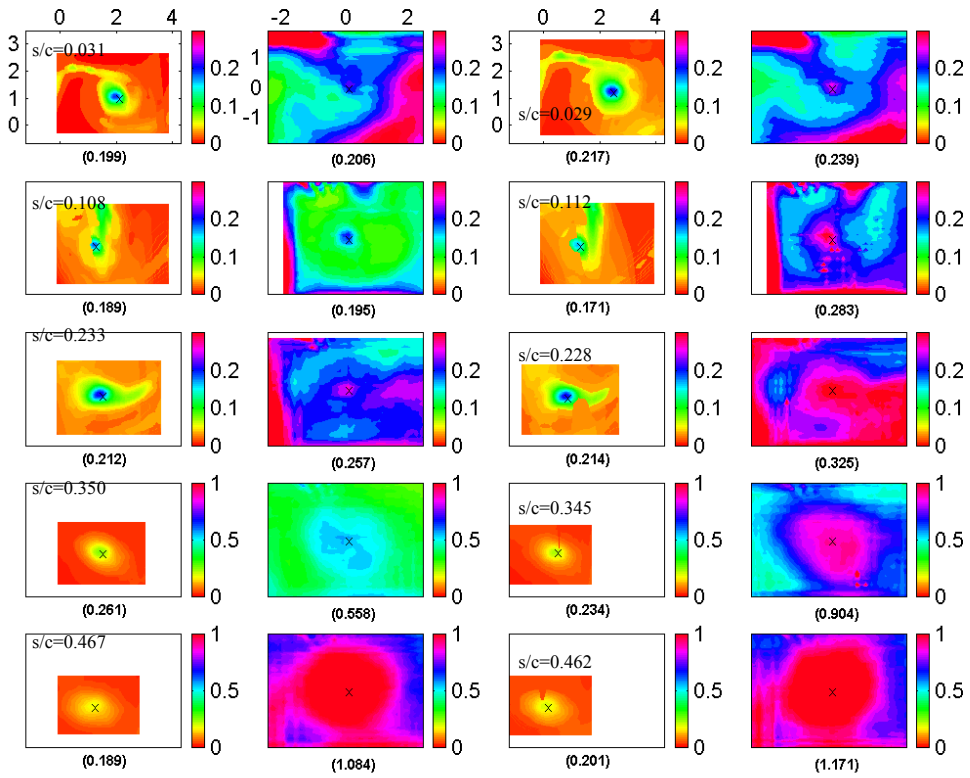

(a) (b) (c) (d)

Figure 20: Velocity fluctuations $\overline{u'^2} + \overline{v'^2}$ for the large rotor. (a, c) are the directly computed fluctuations, and (b, d) are the scaled fluctuations after scaling and shifting . (a, b) correspond to n = 313 rpm, and (c,d) correspond to n = 500 rpm. The value at the center of the primary vortex is also plotted below each figure.

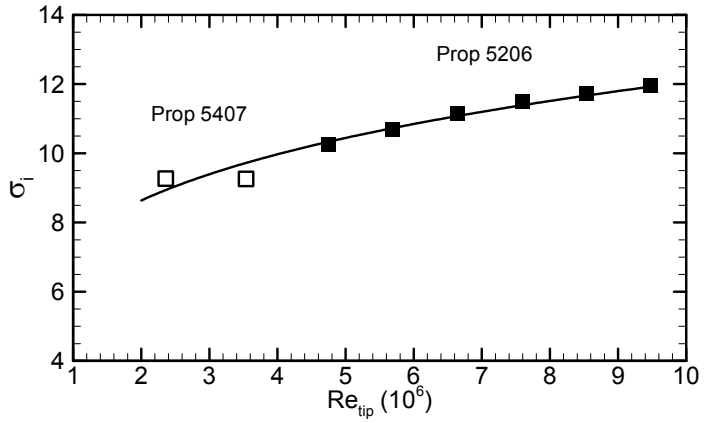

Figure 21: Cavitation inception number, σ_i, as a function of Reynolds number for varying rotor speed. The open symbols are from the small configuration. Inception occurred at $s/c \sim 0.5$.